

LightMedSeg: Lightweight 3D Medical Image Segmentation with Learned Spatial Anchors

Kavyansh Tyagi

National Institute of Technology Kurukshetra, India

123109026@nitkkr.ac.in

Vishwas Rathi*

National Institute of Technology Kurukshetra, India

vishwas@nitkkr.ac.in

Puneet Goyal*

Indian Institute of Technology Ropar, India

puneet@iitrpr.ac.in

Abstract

Accurate and efficient 3D medical image segmentation is essential for clinical AI, where models must remain reliable under stringent memory, latency, and data availability constraints. Transformer-based methods achieve strong accuracy but suffer from excessive parameters, high FLOPs, and limited generalization. We propose LightMedSeg, a modular UNet-style segmentation architecture that integrates anatomical priors with adaptive context modeling. Anchor-conditioned FiLM modulation enables anatomy-aware feature calibration, while a local structural prior module and texture-aware routing dynamically allocate representational capacity to boundary-rich regions. Computational redundancy is minimized through ghost and depthwise convolutions, and multi-scale features are adaptively fused via a learned skip router with anchor-relative spatial position bias. Despite requiring only 0.48M parameters and 14.64 GFLOPs, LightMedSeg achieves segmentation accuracy within a few Dice points of heavy transformer baselines. Therefore, LightMedSeg is a deployable and data-efficient solution for 3D medical image segmentation. Code will be released publicly upon acceptance.

1. Introduction

Deep learning has transformed medical image analysis, driving major gains in the accuracy and reliability of automated diagnostic systems. Within this domain, 3D medical image segmentation is foundational for tumor delineation, organ localization, and treatment planning. Conventional convolutional neural networks (CNNs), such as U-Net and its variants, provide strong baselines through hierarchical local feature extraction. However, their receptive field is in-

herently limited and restricts their ability to model global anatomical dependencies. This issue becomes critical in volumetric data with complex spatial structures and ambiguous boundaries.

To overcome these limitations, transformer based architectures have emerged, leveraging global self-attention to capture semantic coherence and contextual dependencies across entire volumes. Models such as nnFormer [31] and SegFormer3D [20] achieve state-of-the-art performance, often surpassing purely convolutional designs. Yet, these architectures are burdened by large parameter counts, high computational demands, and significant inference latency. Such constraints limit their practicality in real world clinical environments where computational resources are scarce and decisions must be made quickly.

Another persistent gap lies in the uniform way current methods process data. Most approaches overlook valuable anatomical priors, fail to adapt resources to regions of uncertainty or structural ambiguity, and rely on rigid skip connections with static fusion strategies. This undermines multi-scale integration, anatomical fidelity, and ultimately clinical reliability.

We propose LightMedSeg, a U-Net-based architecture designed for efficient 3D medical image segmentation under resource constraints. The model integrates several lightweight mechanisms that collectively achieve strong efficiency-accuracy trade-offs. Specifically, learned spatial anchors provide global context for feature conditioning via FiLM modulation, while an adaptive feature mixing module uses spatial gating to route features through multiple projection heads. In addition, a texture-aware routing mechanism separates high-variation regions from homogeneous areas to guide processing path selection, and a multi-scale skip fusion module learns to combine encoder features across scales rather than relying on fixed connections. Further, spatial position bias derived from anchor-relative distances

**Corresponding authors.

provides explicit spatial guidance during decoding.

Despite its lightweight design, LightMedSeg achieves a competitive segmentation performance with only 0.48M parameters and 14.64 GFLOPs, making LightMedSeg significantly smaller than many traditional transformer-based models. By combining structural priors, adaptive feature routing, and lightweight global context modeling, LightMedSeg offers a practical solution for accurate and efficient volumetric segmentation, narrowing the gap between research prototypes and deployable clinical systems. Our contributions are summarized as follows: (i) we introduce LightMedSeg, a lightweight 3D medical image segmentation architecture having only 0.48M parameters and maintaining competitive accuracy, (ii) we propose a module that utilizes specific spatial anchors and employs global context using anchor conditioned FiLM modulation, (iii) we design a local structural prior module (LSPM) that identifies structurally complex regions and guides features through appropriate processing paths, (iv) we introduce a learned multi scale skip fusion design that adaptively combines encoder features from different scales instead of using fixed U-Net skip connections, and (v) experiments on BraTS and ACDC show that LightMedSeg achieves a strong balance between segmentation accuracy and computational efficiency.

2. Related Work

Recent progress in 3D medical image segmentation has explored convolutional networks, transformers, and hybrid architectures, each aiming to balance accuracy, efficiency, and generalization. CNNs remain effective for local feature capture, transformers excel at global context modeling, and hybrid designs attempt to unify both.

The U-Net [19] and its descendants, including deeply supervised CNNs [32], DenseUNet [2], and volumetric variants such as 3D U-Net [7], V-Net [19], and nnU-Net [13], established the foundation for volumetric segmentation through hierarchical multi-scale features. However, their inherently local receptive fields limit modeling of long-range anatomical dependencies. Extensions via dilated convolutions, pyramid pooling, and attention gates [5, 6, 24] improved context modeling, but still remained bounded by convolutional locality and scaled poorly with deeper backbones [15].

Transformer-based designs introduced global self-attention to address these shortcomings. SETR [30] pioneered a sequence-to-sequence formulation but suffered from spatial detail loss during patch embedding. Hybrid designs such as TransBTS [23], CoTr [29], TransFuse [28], and LoGoNet [14] integrated CNN encoders with transformer modules using cross-attention or deformable attention [25]. While improving local global fusion, these pipelines were computationally heavy and often dataset specific.

Hierarchical transformer-only networks like Swin-UNet [3] and SwinUNETR [9] captured multi-resolution features via shifted window attention, but window partitioning restricted long-range anatomical modeling. Efficient variants such as LeViT-UNet [27] and SegFormer3D [20] reduced parameters with lightweight decoders and streamlined attention, with SegFormer3D reaching 4.51M parameters and 17.5 GFLOPs. Yet these still relied on static skip fusion and struggled under anatomical variation or low contrast conditions.

State-of-the-art designs such as nnFormer [31], which replaced concatenation with skip attention, and UNETR [10], which employed full transformer encoders, significantly improved context capture but at high computational cost. UNETR++ [22] reduced overhead through multi-scale cross skip connections and lightweight decoders, but remained parameter-heavy and reliant on dense supervision.

Despite these advances, existing approaches remain challenged by static feature fusion, large parameterization, and dependence on voxel-level supervision.

In summary, several methods have reduced computational overhead and improved accuracy, they remain limited by rigid fusion, heavy parameter counts, and sensitivity to annotation scarcity. LightMedSeg addresses all three challenges simultaneously, offering anatomically-aware segmentation that is efficient, adaptive, and reliable under real-world constraints.

3. Proposed Method

LightMedSeg is designed for 3D medical image segmentation in resource constraints environment, where memory and compute budgets preclude large transformer-based models. Given an input volume $\mathbf{X} \in \mathbb{R}^{B \times C_{in} \times D \times H \times W}$, the network produces voxel-wise class logits $\hat{\mathbf{Y}} \in \mathbb{R}^{B \times N_{cls} \times D \times H \times W}$.

LightMedSeg follows a U-Net style encoder-decoder design, where computational redundancy is minimized through ghost and depthwise convolutions while introducing structural context through lightweight prior modules. A learned skip router and anchor-relative spatial position bias in the decoder recover fine-grained anatomical detail without increasing model complexity.

The overall architecture comprises five components:(i) a GhostConv3D patch embedding stem that halves spatial resolution and produces modality independent feature maps, (ii) a global anchor detector that predicts sample specific spatial anchors from the input, (iii) a local structural prior module (LSPM) that extracts a texture routing map and a structurally adapted feature map, (iv) a four-stage encoder with anchor-conditioned FiLM modulation and texture-aware routing at each stage, and (v) a symmetric four-stage decoder with learned multi-scale skip fusion,

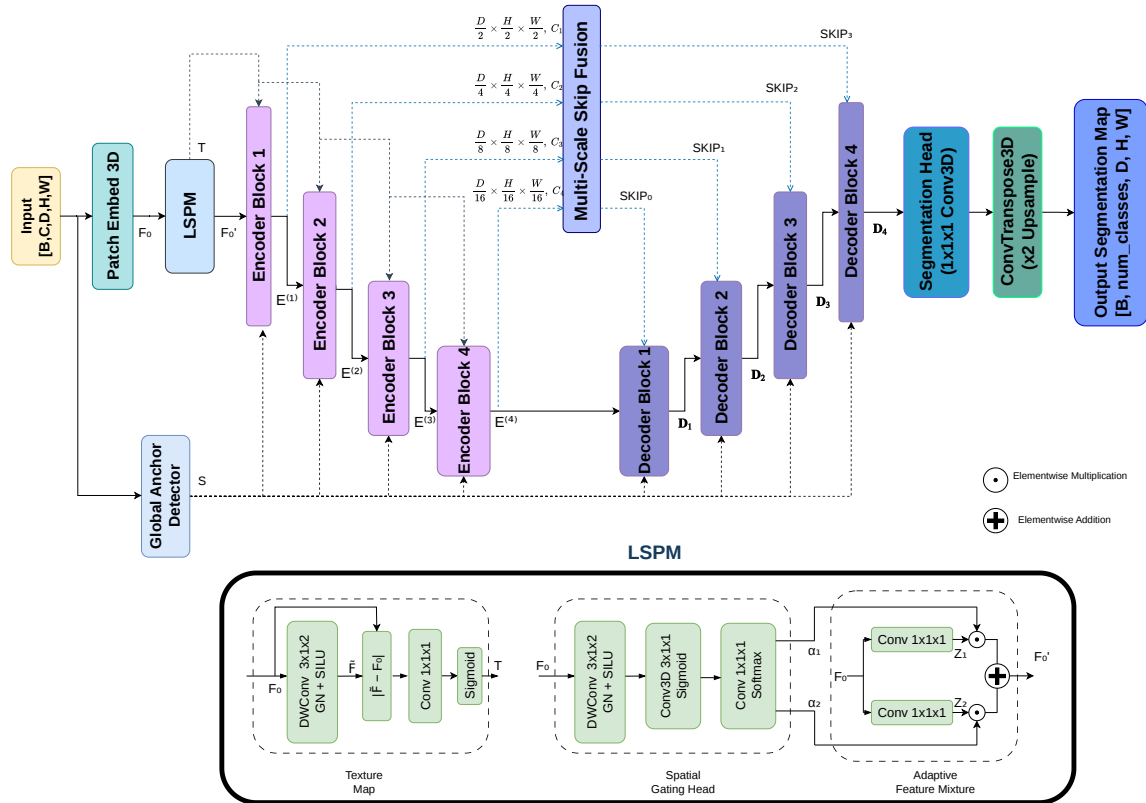


Figure 1. Architecture of **LightMedSeg**. The input volume is first embedded by a stride-2 GhostConv3D stem. The Global Anchor Detector and the Local Structural Prior Module (LSPM) extract spatial anchors \mathbf{S} and a texture routing map \mathbf{T} from the stem features. These priors guide (i) adaptive feature mixing before the encoder, (ii) anchor-conditioned, texture-routed processing at every encoder stage, (iii) multi-scale learned skip fusion, and (iv) an adaptive decoder with content-tied spatial position bias. A final ConvTranspose3D restores voxel-wise class logits at the original resolution.

factored spatial position bias, and adaptive multi path processing. Each component is described in detail below.

3.1. Patch Embedding Stem

The input volume $\mathbf{X} \in \mathbb{R}^{B \times C_{in} \times D \times H \times W}$ has C_{in} channels, corresponding to the number of imaging modalities. Standard 3D patch embedding projects this directly through a dense Conv3D, incurring higher parameters regardless of spatial redundancy. We instead adopt GhostConv3D [8] with ghost ratio $\rho = 2$, which splits feature generation into two steps: a strided Conv3D with kernel size 3 and stride 2 produces half the required output channels from the input as primary features, and a depthwise Conv3D with kernel size 3 and stride 1 synthesizes the remaining half from those primary features as ghost features. The two are concatenated and normalized via Group Normalization with four groups (GN_4), yielding the stem output $\mathbf{F}_0 \in \mathbb{R}^{B \times C_0 \times \frac{D}{2} \times \frac{H}{2} \times \frac{W}{2}}$ with $C_0 = 8$, approximately $2 \times$ fewer parameters and FLOPs than a standard Conv3D stem.

The stride 2 reduction (128^3 to 64^3 for BraTS inputs) re-

duces the memory footprint of all downstream operations and is fully recovered by the four transposed convolution stages in the decoder (Section 3.6). The output is a fixed 8 channel feature volume irrespective of the number of input modalities, providing a consistent representation to all downstream modules.

3.2. Global Anchor Detector

Global context in purely convolutional encoders relies on large receptive fields, which are prohibitively expensive at 3D scale, while attention-based alternatives incur quadratic voxel complexity. We instead propose a lightweight *Global Anchor Detector* that distills global spatial information from the raw input \mathbf{X} into $K = 8$ anchor coordinates, each normalized to $[0, 1]^3$ along the depth, height, and width axes, representing salient spatial locations in the volume. Anchors are predicted without any spatial supervision at a cost of only 8.6K parameters.

The detector uses a three-layer encoder ϕ (Conv3D, GN_4 , SiLU; kernel 3, stride 2, padding 1) that progres-

sively compresses \mathbf{X} into a compact feature volume. A 3D Global Average Pooling layer then collapses spatial dimensions into a per-sample descriptor, passed to a two-layer MLP (hidden width 128, SiLU) that projects to $3K$ logits. A sigmoid activation constrains each coordinate to $[0, 1]$, ensuring all anchors lie within the input volume:

$$\mathbf{S} = \sigma(\text{MLP}(\text{GAP3D}(\phi(\mathbf{X})))) \in [0, 1]^{B \times K \times 3}, \quad (1)$$

where each of the K rows of \mathbf{S} encodes the normalized coordinate (d, h, w) of one predicted anchor. Anchors are sample specific as they adapt to each individual input volume rather than being fixed positional tokens. \mathbf{S} serves two roles downstream: FiLM-based feature modulation at every encoder stage (Section 3.4), and content-adaptive spatial position bias throughout the decoder (Section 3.6).

3.3. Local Structural Prior Module (LSPM)

Standard convolutional encoders apply identical computation to every voxel, wasting capacity on homogeneous interiors while potentially under-serving boundaries. The Local Structural Prior Module (LSPM) addresses this via a lightweight three-branch block operating on the stem output \mathbf{F}_0 , emitting two signals: a per-voxel texture routing map \mathbf{T} consumed by all four encoder stages, and a structurally adapted feature map \mathbf{F}'_0 passed as the encoder’s initial input, at a cost of only 11.7K parameters (2.4% of the model).

The three branches operate in parallel: Branch 1 detects *where* structural complexity exists via high-frequency intensity transitions; Branch 2 estimates *how much* complexity is present in the learned feature space; and Branch 3 consumes this estimate to adaptively blend two parallel feature projections, favouring expressive capacity near boundaries and simpler processing in smooth interiors.

Texture Map (Branch 1): Boundary and interface voxels in medical volumes exhibit sharp local intensity transitions as tissue interiors are largely smooth. To identify these structurally rich regions without a feature pyramid, a $5 \times 5 \times 5$ depthwise convolution where $s=1, p=2, \text{groups}=C_0$, smooths \mathbf{F}_0 . So the absolute residual isolates high frequency content:

$$\tilde{\mathbf{F}} = \text{SiLU}(\text{GN}_4(\text{DWConv3D}(\mathbf{F}_0; k=5, s=1, p=2, \text{groups}=C_0))), \quad (2)$$

$$\mathbf{T} = \sigma\left(\text{Conv}_{1 \times 1 \times 1}\left(\left|\tilde{\mathbf{F}} - \mathbf{F}_0\right|; C_0 \rightarrow 1\right)\right) \in [0, 1]^{B \times 1 \times 64^3}. \quad (3)$$

$\mathbf{T}_{b,d,h,w}$ at boundaries and interfaces. \mathbf{T} is forwarded unchanged to all four encoder stages as a stable routing reference. This branch costs 1K parameters.

Spatial Gating Head (Branch 2): While \mathbf{T} captures high-frequency texture in the input space, it does not directly reflect structural complexity in the learned feature space. We

therefore estimate a complementary per-voxel complexity score \mathbf{G} via a two-layer convolutional head ψ . Two consecutive convolutions with kernel size 3, stride 1 and padding 1, each followed by GN_4 and SiLU, progressively expand \mathbf{F}_0 from C_0 channels to $2C_0$ channels and then collapse to a single-channel output, giving ψ an effective receptive field of $5 \times 5 \times 5$ voxels:

$$\mathbf{G} = \sigma(\psi(\mathbf{F}_0)) \in [0, 1]^{B \times 1 \times 64^3}. \quad (4)$$

Values near 1 indicate structurally complex voxels; values near 0 indicate smooth regions. \mathbf{G} is passed internally to Branch 3, where it is projected to per-voxel expert weights α_1, α_2 via a $1 \times 1 \times 1$ convolution followed by softmax, satisfying $\alpha_{1,r} + \alpha_{2,r} = 1$ at every voxel r . This branch costs 10.5K parameters.

Adaptive Feature Mixer (Branch 3): The stem applies a fixed linear projection uniformly to all voxels, regardless of local complexity. We address this with a soft mixture of two parallel $1 \times 1 \times 1$ expert projections \mathbf{Z}_1 and \mathbf{Z}_2 , each mapping from C_0 to C_0 channels, recombined in spatially varying proportions:

$$\mathbf{F}'_0 = \alpha_1 \odot \mathbf{Z}_1 + \alpha_2 \odot \mathbf{Z}_2 \in \mathbb{R}^{B \times C_0 \times 64^3}. \quad (5)$$

The softmax constraint ensures the full representational budget is redistributed between experts rather than reduced. The $1 \times 1 \times 1$ kernels restrict each expert to channel recombination only, leaving all spatial processing to the encoder. Expert specialization between complex and smooth regions emerges from end-to-end training without explicit supervision, at a cost of only 0.15K parameters.

The LSPM takes $\mathbf{F}_0 \in \mathbb{R}^{B \times C_0 \times 64^3}$ as its sole input and emits $\mathbf{T} \in [0, 1]^{B \times 1 \times 64^3}$ and $\mathbf{F}'_0 \in \mathbb{R}^{B \times C_0 \times 64^3}$ which are fed into the encoder stages.

3.4. Encoder Hierarchy

The encoder is a four-stage hierarchical feature extractor progressively abstracting the input from fine-grained local structure to coarse semantics. At each stage $i \in \{1, 2, 3, 4\}$, three operations are applied: anchor-conditioned GhostConv3D projection via FiLM [21], which scales and shifts feature channels by the learned anchor coordinates; texture-aware dual-branch routing; and SE channel recalibration. Each stage output is stored as skip feature $\mathbf{E}^{(i)}$ before downsampling.

Stages 1 to 3 apply MaxPool3D with kernel size 2 and stride 2 after feature storage to halve all spatial dimensions. The stage 4 retains the bottleneck resolution via an identity mapping, as further downsampling would destroy the spatial detail required by the decoder during reconstruction.

The encoder receives $\mathbf{F}'_0 \in \mathbb{R}^{B \times C_0 \times \frac{D}{2} \times \frac{D}{2} \times \frac{D}{2}}$ from the LSPM as its stage 1 input. Channel widths follow the schedule $C_i \in \{8, 16, 32, 64\}$, doubling at each stage, while spatial resolutions progressively reduce from $\frac{D}{2}$ down to $\frac{D}{4}, \frac{D}{8}$,

and finally $\frac{D}{16}$ along the depth axis (similarly for H and W). The bottleneck representation $\mathbf{E}^{(4)} \in \mathbb{R}^{B \times 64 \times \frac{D}{16} \times \frac{H}{16} \times \frac{W}{16}}$ seeds the decoder.

Purely local convolutional encoders have no mechanism to incorporate global spatial context, which is critical for localizing anatomically specific structures in medical volumes. We therefore condition every encoder stage on the learned spatial anchors via FiLM modulation. The anchor coordinates \mathbf{S} are first flattened into a single vector \mathbf{s} , which is then passed through two independent linear projections $\mathbf{W}_{\gamma,i} \in \mathbb{R}^{C_i \times (K \times 3)}$ and $\mathbf{W}_{\beta,i} \in \mathbb{R}^{C_i \times (K \times 3)}$, whose weights are learned during training, to produce a per-stage scale parameter $\gamma_i = \mathbf{W}_{\gamma,i}\mathbf{s}$ and shift parameter $\beta_i = \mathbf{W}_{\beta,i}\mathbf{s}$, each of dimension C_i , providing one scale and one shift value per feature channel. These modulate the GhostConv3D output at stage i to produce the conditioned feature map $\mathbf{F}_i^{(\text{cond})} \in \mathbb{R}^{B \times C_i \times D_{i-1} \times H_{i-1} \times W_{i-1}}$:

$$\mathbf{F}_i^{(\text{cond})} = (1 + \gamma_i) \otimes \text{GhostConv3D}(\mathbf{F}_{i-1}) + \beta_i, \quad (6)$$

The conditioned features $\mathbf{F}_i^{(\text{cond})}$ are then processed through a texture-aware two-path routing step, where the routing is governed by \mathbf{T}_i , generated by texture map \mathbf{T} trilinearly resampled to the current stage resolution $(D_{i-1}, H_{i-1}, W_{i-1})$. Rather than applying a single convolution uniformly across all voxels, the two paths specialize: the detail-preserving path produces $\mathbf{Z}_i^{\text{detail}} \in \mathbb{R}^{B \times C_i \times D_{i-1} \times H_{i-1} \times W_{i-1}}$ by capturing fine-grained boundary structure via a depthwise convolution over a local spatial neighborhood, while the smoothing path produces $\mathbf{Z}_i^{\text{smooth}} \in \mathbb{R}^{B \times C_i \times D_{i-1} \times H_{i-1} \times W_{i-1}}$ by handling homogeneous interior regions cheaply via a $1 \times 1 \times 1$ pointwise convolution. Formally:

$$\mathbf{Z}_i^{\text{detail}} = \text{SiLU}\left(\text{GN}_4\left(\text{DWConv}_{33}\left(\mathbf{F}_i^{(\text{cond})}; s=1, p=1, \text{groups}=C_i\right)\right)\right), \quad (7)$$

$$\mathbf{Z}_i^{\text{smooth}} = \text{Conv}_{1 \times 1 \times 1}\left(\mathbf{F}_i^{(\text{cond})}; C_i \rightarrow C_i, s=1\right), \quad (8)$$

and blend them continuously using \mathbf{T}_i as a soft gate:

$$\mathbf{F}_i^{(\text{tex})} = \mathbf{T}_i \otimes \mathbf{Z}_i^{\text{detail}} + (1 - \mathbf{T}_i) \otimes \mathbf{Z}_i^{\text{smooth}}, \quad (9)$$

where $\mathbf{T}_i \in [0, 1]^{B \times 1 \times D_{i-1} \times H_{i-1} \times W_{i-1}}$ is broadcast over C_i channels.

Finally, after the two-path routing, a Squeeze-and-Excitation block [11] recalibrates the per-channel responses of $\mathbf{F}_i^{(\text{tex})}$ via global average pooling and a bottleneck MLP:

$$\mathbf{E}^{(i)} = \sigma\left(\mathbf{W}_{2,i} \cdot \text{SiLU}\left(\mathbf{W}_{1,i} \cdot \text{GAP3D}\left(\mathbf{F}_i^{(\text{tex})}\right)\right)\right) \otimes \mathbf{F}_i^{(\text{tex})}, \quad (10)$$

where $\mathbf{W}_{1,i} \in \mathbb{R}^{b_i \times C_i}$, $\mathbf{W}_{2,i} \in \mathbb{R}^{C_i \times b_i}$, and $b_i = \max(4, \lfloor C_i/8 \rfloor)$. The minimum bottleneck width of 4 prevents channel-agnostic collapse at the narrow early stages. $\mathbf{E}^{(i)}$ is stored for skip fusion and passed through Max-Pool3D to seed stage $i+1$.

3.5. Multi-Scale Skip Fusion

Standard U-Net skip connections forward only same-scale encoder features, discarding all cross-scale context. Inspired by full-scale skip designs [12], we replace this with a learned router that adaptively combines all four encoder stages at each decoder level via per-voxel softmax weights, at a cost of only 24K parameters.

Since encoder stages produce features of different widths ($C_i \in \{8, 16, 32, 64\}$), each $\mathbf{E}^{(i)}$ is first projected to a common width of 64 via a $1 \times 1 \times 1$ convolution before routing for $i \in \{1, 2, 3, 4\}$:

$$\hat{\mathbf{E}}^{(i)} = \text{Conv}_{1 \times 1 \times 1}\left(\mathbf{E}^{(i)}\right) \in \mathbb{R}^{B \times 64 \times D_{i-1} \times H_{i-1} \times W_{i-1}}, \quad (11)$$

At the two higher-resolution decoder stages ($j = 3, 4$), concatenating all four aligned maps is expensive in memory. Only the spatially corresponding encoder feature map $\mathbf{E}^{(S-1-j)}$ is therefore projected to C_j channels and trilinearly upsampled to (D_j, H_j, W_j) , where the index $(M - 1 - j)$ selects encoder stage 1 for $j = 3$ and the stem output for $j = 4$, and this single aligned map is used directly as **SKIP** $_j$ at those stages.

At the two lower-resolution stages where $j = 1$ and $j = 2$, the full learned router is activated. Each $\hat{\mathbf{E}}^{(i)}$ is trilinearly upsampled to (D_j, H_j, W_j) and all four are concatenated into a tensor of 256 channels. A two-layer CNN controller consisting of two $1 \times 1 \times 1$ convolutions with a SiLU activation in between, first reducing from 256 to 64 channels and then projecting to M channels, predicts per-voxel logits $\ell_{j,i,r}$ over encoder stages. Softmax normalization gives routing weights and the fused signal:

$$\alpha_{j,i,r} = \frac{e^{\ell_{j,i,r}}}{\sum_{i'=1}^M e^{\ell_{j,i',r}}}, \quad \sum_{i=1}^M \alpha_{j,i,r} = 1, \quad (12)$$

$$\mathbf{SKIP}_j = \sum_{i=1}^M \alpha_{j,i} \odot \hat{\mathbf{E}}_j^{(i)} \in \mathbb{R}^{B \times 64 \times D_j \times H_j \times W_j}, \quad (13)$$

where $\alpha_{j,i} \in \mathbb{R}^{B \times 1 \times D_j \times H_j \times W_j}$ is broadcast over 64 channels. A final $1 \times 1 \times 1$ convolution projects the fused features from 64 channels down to C_j channels, yielding **SKIP** $_j \in \mathbb{R}^{B \times C_j \times D_j \times H_j \times W_j}$, which is consumed by decoder stage j .

3.6. Adaptive Decoder

Standard convolutional decoders apply uniform spatial operations across all positions and lack awareness of anatomically significant structures. We address both limitations through a four-stage decoder combining anchor-relative spatial position bias, multi-scale skip fusion, and per-voxel adaptive path selection.

The decoder is seeded by a $1 \times 1 \times 1$ bottleneck projection of $\mathbf{E}^{(4)}$, producing $\mathbf{F}_{\text{dec}} \in \mathbb{R}^{B \times 64 \times \frac{D}{16} \times \frac{H}{16} \times \frac{W}{16}}$ as input to the first stage. At each stage $j \in \{1, 2, 3, 4\}$, three operations are applied sequentially by position-biased upsampling and skip fusion, adaptive multi-path processing, and SE channel recalibration. Channel widths follow a mirrored schedule $C_j \in \{64, 32, 16, 8\}$, halving as resolution doubles. The stage input is upsampled by a $2 \times 2 \times 2$ transposed convolution, yielding $\mathbf{U}_j \in \mathbb{R}^{B \times C_j \times D_j \times H_j \times W_j}$.

Since transposed convolutions carry no anatomical awareness, we add a Spatial Position Bias $\mathbf{SPB}_j \in \mathbb{R}^{B \times C_j \times D_j \times H_j \times W_j}$ to \mathbf{U}_j before skip fusion. Naively storing the full 3D displacement $(\mathbf{r} - \mathbf{s}_k)$, where $\mathbf{r} = (d, h, w) \in \mathbb{Z}^3$ is a voxel coordinate and $\mathbf{s}_k \in [0, 1]^3$ is the normalized anchor location. This would require a $B \times 3K \times D_j \times H_j \times W_j$ tensor. We instead decompose it axis-by-axis and reconstruct via broadcasting, reducing peak memory by 3 times.

We construct a per voxel signed distance map $\mathbf{P}_{j,k} \in \mathbb{R}^{D_j \times H_j \times W_j}$, where each entry $\mathbf{P}_{j,k}[d, h, w]$ stores the cumulative signed offset of voxel (d, h, w) from anchor k along all three spatial axes. For a voxel at integer index (d, h, w) with $d \in \{0, \dots, D_j - 1\}$, $h \in \{0, \dots, H_j - 1\}$, $w \in \{0, \dots, W_j - 1\}$, it is given as:

$$\mathbf{P}_{j,k}[d, h, w] = \left(\frac{d}{D_j} - s_{k,d} \right) + \left(\frac{h}{H_j} - s_{k,h} \right) + \left(\frac{w}{W_j} - s_{k,w} \right) \quad (14)$$

which decomposes the full 3D displacement into three independent 1D arrays having one per axis and are summed elementwise.

Stacking over all K anchors gives a $B \times K \times D_j \times H_j \times W_j$ volume, which is projected to C_j channels via a $1 \times 1 \times 1$ convolution to produce \mathbf{SPB}_j (Eq. 15). Unlike fixed sinusoidal or learnable grid encodings, \mathbf{SPB}_j changes with every input volume, giving the decoder dynamic positional awareness tied to the predicted anchor locations \mathbf{S} .

$$\mathbf{SPB}_j = \text{Conv}_{1 \times 1 \times 1}(\text{stack}(\{\mathbf{P}_{j,k}\}_{k=1}^K, \text{dim}=1); K \rightarrow C_j, s=1) \in \mathbb{R}^{B \times C_j \times D_j \times H_j \times W_j}, \quad (15)$$

The position biased upsampled features and the encoder skip signal \mathbf{SKIP}_j are concatenated and passed through a $\text{Conv}_{1 \times 1 \times 1}$ to produce the fused representation:

$$\mathbf{D}_j^{(\text{in})} = \text{Conv}_{1 \times 1 \times 1}(\text{Concat}[\mathbf{U}_j + \mathbf{SPB}_j, \mathbf{SKIP}_j]) \quad (16)$$

to produce fused representation $\mathbf{D}_j^{(\text{in})}$, which recalibrates the fused channels before multi-path processing.

The fused representation is processed by three complementary parallel branches, each applying a different spatial transformation. A shared $1 \times 1 \times 1$ convolution produces per-voxel soft blending weights $\pi_{j,p}$ via softmax:

$$\pi_{j,p} = \text{softmax}_p\left(\text{Conv}_{1 \times 1 \times 1}\left(\mathbf{D}_j^{(\text{in})}; C_j \rightarrow P\right)\right), \quad (17)$$

where $\sum_{p=1}^P \pi_{j,p,r} = 1$ at every voxel \mathbf{r} . The final gated output is their weighted sum:

$$\mathbf{D}_j^{(\text{gated})} = \sum_{p=1}^P \pi_{j,p} \odot \mathcal{F}_p\left(\mathbf{D}_j^{(\text{in})}\right), \quad (18)$$

where each \mathcal{F}_p denotes one of the three branches:

$$\mathcal{F}_1\left(\mathbf{D}_j^{(\text{in})}\right) = \text{SiLU}\left(\text{GN}_4\left(\text{DWConv3D}_3\left(\mathbf{D}_j^{(\text{in})}\right)\right)\right), \quad (19)$$

$$\mathcal{F}_2\left(\mathbf{D}_j^{(\text{in})}\right) = \text{SiLU}\left(\text{GN}_4\left(\text{GhostConv3D}_{3, \rho=2}\left(\mathbf{D}_j^{(\text{in})}\right)\right)\right), \quad (20)$$

$$\mathcal{F}_3\left(\mathbf{D}_j^{(\text{in})}\right) = \text{SiLU}\left(\text{GN}_4\left(\text{Conv}_{1 \times 1 \times 1}\left(\mathbf{D}_j^{(\text{in})}\right)\right)\right). \quad (21)$$

\mathcal{F}_1 (depthwise Conv3D, kernel 3, groups C_j) aggregates local neighbourhoods, making it effective at organ boundaries; \mathcal{F}_2 (GhostConv3D, kernel 3, $\rho = 2$) captures multi-scale context at half the cost of a standard Conv3D; and \mathcal{F}_3 ($1 \times 1 \times 1$ conv) performs pure channel mixing suited to smooth homogeneous regions. The blending weights allow each voxel to adaptively select its own mixture of local, multi-scale, and channel-only processing.

The gated output $\mathbf{D}_j^{(\text{gated})}$ is then passed through a Squeeze-and-Excitation block with bottleneck width $b_j = \max(4, \lfloor C_j/8 \rfloor)$, which recalibrates channel importance to produce the final stage output $\mathbf{D}_j \in \mathbb{R}^{B \times C_j \times D_j \times H_j \times W_j}$.

The four stages progressively restore resolution from $\frac{D}{16}$ through $\frac{D}{8}$, $\frac{D}{4}$, and $\frac{D}{2}$ back to the full input resolution D , with the final output $\mathbf{D}_4 \in \mathbb{R}^{B \times C_0 \times D \times H \times W}$ carrying C_0 (here $C_0 = 8$) channels.

A $1 \times 1 \times 1$ convolution first maps \mathbf{D}_4 to N_{cls} channels, followed by a $2 \times 2 \times 2$ transposed convolution with stride 2 that restores the full input resolution, yielding voxel-wise class logits $\hat{\mathbf{Y}} \in \mathbb{R}^{B \times N_{\text{cls}} \times D \times H \times W}$, passed to the loss at training time and to arg max at inference.

3.7. Training Objective

We train with a weighted combination of Dice, cross-entropy, and boundary losses:

$$\mathcal{L} = \mathcal{L}_{\text{Dice}} + \mathcal{L}_{\text{CE}} + 0.5 \mathcal{L}_{\text{Bdry}}. \quad (22)$$

All three terms are weighted by the inverse voxel frequency $w_c = |\Omega| / (N_{\text{cls}} \cdot \sum_{\mathbf{r}} y_{c,\mathbf{r}})$ to counteract foreground-background imbalance. $\mathcal{L}_{\text{Dice}}$ optimizes region overlap; \mathcal{L}_{CE} provides per-voxel calibration. $\mathcal{L}_{\text{Bdry}}$ applies a masked binary cross-entropy restricted to voxels within a morphologically dilated ($d = 3$, ℓ_∞ norm) class-boundary region M , normalized by $|M|$ to keep gradient magnitude consistent across varying tumor sizes.

4. Experimental Results

We evaluate the proposed model, LightMedSeg, against state-of-the-art 3D medical image segmentation methods on two widely used volumetric benchmarks: BraTS (Brain Tumor Segmentation) [18] and ACDC (Automatic Cardiac Diagnosis Challenge) [1]. To ensure fair comparability with prior work, we follow the training and preprocessing protocols of nnFormer [31], including dataset splits, intensity normalization, cropping and evaluation metrics. No external data sources, pretraining, or auxiliary datasets are used.

We train LightMedSeg from scratch for 300 epochs with a batch size of 8 for BraTS and ACDC. During training, random 3D crops of size $128 \times 128 \times 128$ voxels are extracted from the volumes. BraTS contains 411 training and 73 testing cases. Here, each modality is normalized via per volume $Z - score$. For ACDC intensities are clipped to the 0.5–99.5 percentile range and linearly rescaled to $[0,1]$. We follow the official dataset splits and apply standard 3D data augmentation, including random flipping, rotation, and Gaussian noise. The model parameters are optimized using the AdamW optimizer [17], with an initial learning rate of 2×10^{-4} , weight decay 1×10^{-5} , and default betas (0.9, 0.999). A cosine annealing scheduler [16] is applied with a minimum learning rate of 1×10^{-9} and $T_{\text{max}} = 100$ epochs, following a short warmup.

The performance is reported using Dice score as the primary metric for the relative comparisons of models. Tables 1 and 2 present the results on BraTS and ACDC, respectively. On BraTS, LightMedSeg achieves an average Dice score of 83.4% using only 0.48M parameters, compared to nnFormer, which achieves 86.4% with 150M parameters over $50\times$ larger. On ACDC, LightMedSeg achieves 91.24%, which is close to the best performer, UNETR++, with 92.83%.

Figures 2 and 3 visualize representative predictions. On BraTS, our model accurately captures small enhancing tumor regions and irregular boundaries, while on ACDC it produces precise LV and myocardium masks with sharp boundaries. These results indicate strong clinical potential under both limited compute and limited data regimes.

As shown in Table 3, LightMedSeg achieves the lowest parameter count 0.48M and FLOPs 14.64 GFLOPs among all compared architectures. It is $9\times$ more compact than the next most efficient baseline SegFormer3D and over $88\times$

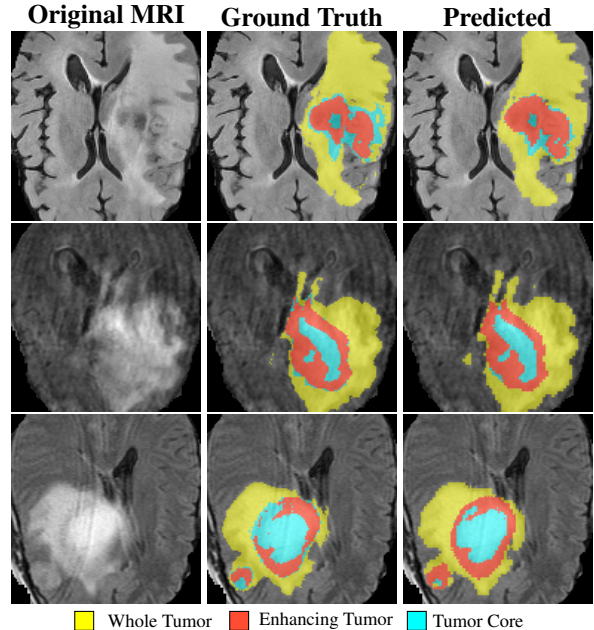


Figure 2. Visual comparison of original MRI, ground truth, and predicted segmentation for four representative BraTS cases.

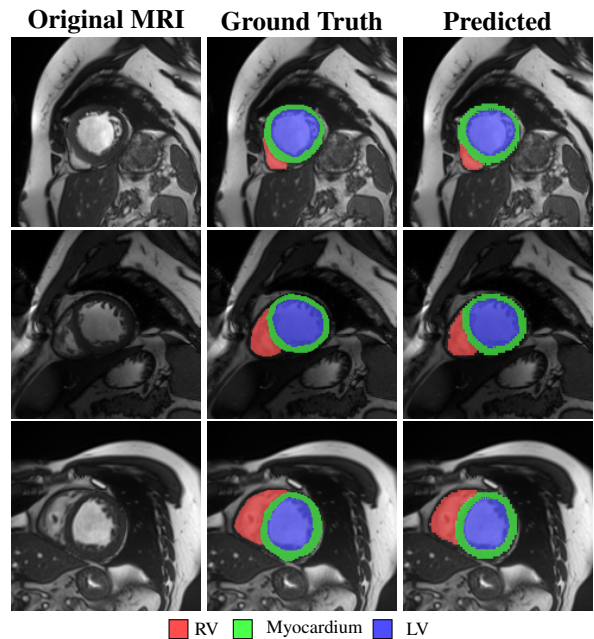


Figure 3. Visual comparison of original MRI, ground truth, and predicted segmentation for four ACDC cases.

smaller than UNETR++. Owing to the absence of self-attention and extensive use of depthwise and ghost convolutions, LightMedSeg processes a 128^3 volume in approximately 13.7 ms on a single NVIDIA RTX 5080 GPU and 505.4 ms on Ryzen 9 9950x CPU, demonstrating suitability

Table 1. Comparison of various methods on the BraTS dataset using average Dice score. Bold values represent the best performance, while underlined values indicate the second best results. Here, the number of parameters (denoted as 'params') is reported in millions.

Methods	Param	Avg %	Whole Tumor ↑	Enhancing Tumor ↑	Tumor Core ↑
nnFormer[31]	150.5	86.4	91.3	81.8	86.0
Segformer3D[20]	4.5	82.1	89.9	74.2	82.2
UNETR[10]	92.49	71.1	78.9	58.5	76.1
TransBTS[23]	–	69.6	77.9	57.4	73.5
CoTr[26]	41.9	68.3	74.6	55.7	74.8
CoTr w/o CNN Encoder[26]	–	64.4	71.2	52.3	69.8
TransUNet[4]	96.07	64.4	70.6	54.2	68.4
SETR MLA[29]	310.5	63.9	69.8	55.4	66.5
SETR PUP[29]	318.31	63.8	69.6	54.9	67.0
SETR NUP[29]	305.67	63.7	69.7	54.4	66.9
LightMedSeg(Ghost Conv)	0.48	83.4	89.8	77.0	83.5
LightMedSeg(Standard Conv)	0.66	<u>84.8</u>	<u>90.9</u>	<u>80.3</u>	<u>83.9</u>

Table 2. Comparison on ACDC dataset (avg. Dice score). Params in millions. **Bold**: best, underline: second best.

Method	Params	Avg%↑	RV	Myo	LV
nnFormer [31]	150.5	<u>92.06</u>	90.94	<u>89.58</u>	95.65
Segformer3D [20]	4.5	90.96	88.50	88.86	95.53
LeViT-UNet [27]	52.17	90.32	89.55	87.64	93.76
SwinUNet [3]	–	90.00	88.55	85.62	95.83
TransUNet [4]	96.07	89.71	88.86	85.54	95.73
UNETR [10]	92.49	88.61	85.29	86.52	94.02
R50-ViT [4]	86.00	87.57	86.07	81.88	94.75
ViT-CUP [4]	86.00	81.45	81.46	70.71	92.18
UNETR++ [22]	42.96	92.83	<u>91.89</u>	90.61	96.00
LightMedSeg (Ghost Conv)	0.48	91.24	91.77	86.24	<u>95.72</u>
LightMedSeg (Standard Conv)	0.66	91.81	92.17	87.78	95.47

Table 3. Comparison of LightMedSeg with state-of-the-art methods in terms of model size, computational complexity, and peak memory. Measured on a BraTS-sized input ($1 \times 4 \times 128^3$); – indicates unavailable data.

Architecture	Params (M)	FLOPs (G)	Mem (MB)
nnFormer [31]	150.5	213.4	12902
UNETR [10]	92.49	75.76	3379
SwinUNETR [9]	62.83	384.2	20173
UNETR++ [22]	42.96	70.1	<u>2458</u>
SegFormer3D [20]	<u>4.51</u>	<u>17.5</u>	–
LightMedSeg	0.48	14.64	1174

for real-time clinical deployment.

Table 4 shows the ablation results. These results highlight that LSPM contributes the most to segmentation accuracy, indicating that explicitly modeling structural com-

Table 4. Component ablation on BraTS (Avg. Dice). K denotes the number of anatomical anchors.

Configuration	Avg Dice
Full Model	83.43
w/o LSPM	80.50 (−2.93)
w/o Anchors	81.93 (−1.50)
w/o Skip Router	82.27 (−1.16)
w/o GhostConv3D	84.81 (+1.38)
$K=8$ (default)	83.43 (0.48M)
$K=16$	83.64 (0.49M)
$K=32$	84.16 (0.52M)

plexity is crucial for lightweight architectures. Removing the LSPM causes the largest drop (−2.93 Dice), confirming structural priors and texture-aware routing as the most critical choices; disabling the Global Anchor Detector and the learned skip router cost −1.50 and −1.16 Dice respectively. Removing GhostConv3D recovers +1.38 Dice at the cost of more parameters. k is the number of anatomical anchors, we default to $K=8$ giving us 83.43 Dice over $K=32$ with 84.16, to best suit our efficiency target.

5. Conclusion

We presented LightMedSeg, a compact 3D medical image segmentation network that achieves accuracy competitive with models orders of magnitude larger. By combining anchor conditioned FiLM modulation, local structural priors, texture-aware routing, and learned multi-scale skip fusion, the model delivers strong performance on BraTS and ACDC while remaining deployable under strict memory and compute constraints. Future work will explore semi-supervised and multi-institutional settings, as well as extension to additional imaging modalities.

References

- [1] Olivier Bernard, Alain Lalande, Clement Zotti, Frederick Cervenansky, Xin Yang, and et al Heng. Deep learning techniques for automatic mri cardiac multi-structures segmentation and diagnosis: Is the problem solved? *IEEE transactions on medical imaging*, 37(11):2514–2525, 2018. 7
- [2] Sijing Cai, Yunxian Tian, Harvey Lui, Haishan Zeng, Yi Wu, and Guannan Chen. Dense-unet: a novel multiphoton in vivo cellular image segmentation model based on a convolutional neural network. *Quantitative Imaging in Medicine and Surgery*, 10(6), 2020. 2
- [3] Hu Cao, Yueyue Wang, Joy Chen, Dongsheng Jiang, Xiaopeng Zhang, Qi Tian, and Manning Wang. *Swin-Unet: Unet-Like Pure Transformer for Medical Image Segmentation*, pages 205–218. Springer, 2023. 2, 8
- [4] Jieneng Chen, Yongyi Lu, Qihang Yu, Xiangde Luo, Ehsan Adeli, Yan Wang, Le Lu, Alan L. Yuille, and Yuyin Zhou. Transunet: Transformers make strong encoders for medical image segmentation. *CoRR*, abs/2102.04306, 2021. 8
- [5] Linwei Chen, Lin Gu, Dezhi Zheng, and Ying Fu. Frequency-adaptive dilated convolution for semantic segmentation. In *Proceedings of the IEEE/CVF Conference on Computer Vision and Pattern Recognition*, pages 3414–3425, 2024. 2
- [6] Tong Chen, Haojie Liu, Zhan Ma, Qiu Shen, Xun Cao, and Yao Wang. End-to-end learnt image compression via non-local attention optimization and improved context modeling. *IEEE Transactions on Image Processing*, 30:3179–3191, 2021. 2
- [7] Özgün Çiçek, Ahmed Abdulkadir, Soeren S. Lienkamp, Thomas Brox, and Olaf Ronneberger. 3D U-Net: Learning dense volumetric segmentation from sparse annotation. In *Medical Image Computing and Computer-Assisted Intervention – MICCAI 2016*, pages 424–432. Springer, 2016. 2
- [8] Kai Han, Yunhe Wang, Qi Tian, Jianyuan Guo, Chunjing Xu, and Chang Xu. Ghostnet: More features from cheap operations. In *Proceedings of the IEEE/CVF conference on computer vision and pattern recognition*, pages 1580–1589, 2020. 3
- [9] Ali Hatamizadeh, Vishwesh Nath, Yucheng Tang, Dong Yang, Holger R. Roth, and Daguang Xu. Swin unetr: Swin transformers for semantic segmentation of brain tumors in mri images. In *Brainlesion: Glioma, Multiple Sclerosis, Stroke and Traumatic Brain Injuries*, pages 272–284, Cham, 2022. Springer International Publishing. 2, 8
- [10] Ali Hatamizadeh, Yucheng Tang, Vishwesh Nath, Dong Yang, Andriy Myronenko, Bennett Landman, Holger R. Roth, and Daguang Xu. Unetr: Transformers for 3d medical image segmentation. In *2022 IEEE/CVF Winter Conference on Applications of Computer Vision (WACV)*, pages 1748–1758, 2022. 2, 8
- [11] Jie Hu, Li Shen, and Gang Sun. Squeeze-and-excitation networks. In *Proceedings of the IEEE/CVF Conference on Computer Vision and Pattern Recognition (CVPR)*, pages 7132–7141, 2018. 5
- [12] Huimin Huang, Lanfen Lin, Ruofeng Tong, Hongjie Hu, Qiaowei Zhang, Yutaro Iwamoto, Xianhua Han, Yen-Wei Chen, and Jian Wu. UNet 3+: A full-scale connected UNet for medical image segmentation. In *IEEE International Conference on Acoustics, Speech and Signal Processing (ICASSP)*, pages 1055–1059, 2020. 5
- [13] Fabian Isensee, Paul F. Jaeger, Simon A. A. Kohl, Jens Petersen, and Klaus H. Maier-Hein. nnu-net: a self-configuring method for deep learning-based biomedical image segmentation. *Nature Methods*, 18(2):203–211, 2021. 2
- [14] Amin Karimi Monsefi, Payam Karisani, Mengxi Zhou, Stacey Choi, Nathan Doble, Heng Ji, Srinivasan Parthasarathy, and Rajiv Ramnath. Masked logonet: Fast and accurate 3d image analysis for medical domain. In *Proceedings of the 30th ACM SIGKDD Conference on Knowledge Discovery and Data Mining*, pages 1348–1359, 2024. 2
- [15] Xiaomeng Li, Hao Chen, Xiaojuan Qi, Qi Dou, Chi-Wing Fu, and Pheng-Ann Heng. H-denseunet: Hybrid densely connected unet for liver and liver tumor segmentation from CT volumes. *CoRR*, abs/1709.07330, 2017. 2
- [16] Ilya Loshchilov and Frank Hutter. SGDR: stochastic gradient descent with restarts. *CoRR*, abs/1608.03983, 2016. 7
- [17] Ilya Loshchilov and Frank Hutter. Fixing weight decay regularization in adam. *CoRR*, abs/1711.05101, 2017. 7
- [18] Bjoern H. Menze, Andras Jakab, Stefan Bauer, Jayashree Kalpathy-Cramer, Keyvan Farahani, Justin Kirby, Yuliya Burren, Nicole Porz, Johannes Slotboom, Roland Wiest, and Koen Van Leemput. The multimodal brain tumor image segmentation benchmark (BRATS). *IEEE Transactions on Medical Imaging*, 34(10):1993–2024, 2015. 7
- [19] Fausto Milletari, Nassir Navab, and Seyed-Ahmad Ahmadi. V-net: Fully convolutional neural networks for volumetric medical image segmentation. In *2016 Fourth International Conference on 3D Vision (3DV)*, pages 565–571, 2016. 2
- [20] Shehan Perera, Pouyan Navard, and Alper Yilmaz. SegFormer3D: an Efficient Transformer for 3D Medical Image Segmentation. In *2024 IEEE/CVF Conference on Computer Vision and Pattern Recognition Workshops (CVPRW)*, pages 4981–4988, Los Alamitos, CA, USA, 2024. IEEE Computer Society. 1, 2, 8
- [21] Ethan Perez, Florian Strub, Harm de Vries, Vincent Dumoulin, and Aaron Courville. FiLM: Visual reasoning with a general conditioning layer. In *Proceedings of the AAAI Conference on Artificial Intelligence*, 2018. 4
- [22] Abdelrahman Shaker, Muhammad Maaz, Hanoona Rasheed, Salman Khan, Ming-Hsuan Yang, and Fahad Shahbaz Khan. Unetr++: Delving into efficient and accurate 3d medical image segmentation. *IEEE Transactions on Medical Imaging*, 43(9):3377–3390, 2024. 2, 8
- [23] Wenxuan Wang, Chen Chen, Meng Ding, Hong Yu, Sen Zha, and Jianguyun Li. Transbts: Multimodal brain tumor segmentation using transformer. In *Medical Image Computing and Computer Assisted Intervention – MICCAI 2021*, pages 109–119, Cham, 2021. Springer International Publishing. 2, 8
- [24] Yu-Huan Wu, Yun Liu, Xin Zhan, and Ming-Ming Cheng. P2t: Pyramid pooling transformer for scene understanding. *IEEE transactions on pattern analysis and machine intelligence*, 45(11):12760–12771, 2022. 2

- [25] Zhuofan Xia, Xuran Pan, Shiji Song, Li Erran Li, and Gao Huang. Vision transformer with deformable attention. In *Proceedings of the IEEE/CVF conference on computer vision and pattern recognition*, pages 4794–4803, 2022. [2](#)
- [26] Yutong Xie, Jianpeng Zhang, Chunhua Shen, and Yong Xia. Cotr: Efficiently bridging CNN and transformer for 3d medical image segmentation. *CoRR*, abs/2103.03024, 2021. [8](#)
- [27] Guoping Xu, Xingrong Wu, Xuan Zhang, and Xinwei He. Levit-unet: Make faster encoders with transformer for medical image segmentation. *CoRR*, abs/2107.08623, 2021. [2](#), [8](#)
- [28] Yundong Zhang, Huiye Liu, and Qiang Hu. Transfuse: Fusing transformers and cnns for medical image segmentation. In *International conference on medical image computing and computer-assisted intervention*, pages 14–24. Springer, 2021. [2](#)
- [29] Sixiao Zheng, Jiachen Lu, Hengshuang Zhao, Xiatian Zhu, Zekun Luo, Yabiao Wang, Yanwei Fu, Jianfeng Feng, Tao Xiang, Philip H. S. Torr, and Li Zhang. Rethinking semantic segmentation from a sequence-to-sequence perspective with transformers. *CoRR*, abs/2012.15840, 2020. [2](#), [8](#)
- [30] Sixiao Zheng, Jiachen Lu, Hengshuang Zhao, Xiatian Zhu, Zekun Luo, Yabiao Wang, Yanwei Fu, Jianfeng Feng, Tao Xiang, Philip HS Torr, et al. Rethinking semantic segmentation from a sequence-to-sequence perspective with transformers. In *Proceedings of the IEEE/CVF conference on computer vision and pattern recognition*, pages 6881–6890, 2021. [2](#)
- [31] Hong-Yu Zhou, Jiansen Guo, Yinghao Zhang, Xiaoguang Han, Lequan Yu, Liansheng Wang, and Yizhou Yu. nn-former: Volumetric medical image segmentation via a 3d transformer. *IEEE Transactions on Image Processing*, 32: 4036–4045, 2023. [1](#), [2](#), [7](#), [8](#)
- [32] Qikui Zhu, Bo Du, Baris Turkbey, Peter L. Choyke, and Pingkun Yan. Deeply-supervised cnn for prostate segmentation. In *2017 International Joint Conference on Neural Networks (IJCNN)*, pages 178–184, 2017. [2](#)